

Demonstration of a non-Abelian geometric controlled-Not gate in a superconducting circuit

KAI XU^{1,2}, WEN NING³, XIN-JIE HUANG³, PEI-RONG HAN³, HEKANG LI², ZHEN-BIAO YANG^{3,4},
DONGNING ZHENG^{1,2}, HENG FAN^{1,2,5}, AND SHI-BIAO ZHENG^{3,6}

¹Institute of Physics and Beijing National Laboratory for Condensed Matter Physics, Chinese Academy of Sciences, Beijing 100190, China

²CAS Center for Excellence in Topological Quantum Computation, University of Chinese Academy of Sciences, Beijing 100190, China

³Fujian Key Laboratory of Quantum Information and Quantum Optics, College of Physics and Information Engineering, Fuzhou University, Fuzhou, Fujian 350108, China

⁴zbyang@fzu.edu.cn

⁵hfan@iphy.ac.cn

⁶t96034@fzu.edu.cn

Compiled June 29, 2021

Holonomies, arising from non-Abelian geometric transformations of quantum states in Hilbert space, offer a promising way for quantum computation. These holonomies are not commutable and thus can be used for the realization of a universal set of quantum logic gates, where the global geometric feature may result in some noise-resilient advantages. Here we report the first on-chip realization of a non-Abelian geometric controlled-Not gate in a superconducting circuit, which is a building block for constructing a holonomic quantum computer. The conditional dynamics is achieved in an all-to-all connected architecture involving multiple frequency-tunable superconducting qubits controllably coupled to a resonator; a holonomic gate between any two qubits can be implemented by tuning their frequencies on resonance with the resonator and applying a two-tone drive to one of them. This gate represents an important step towards the all-geometric realization of scalable quantum computation on a superconducting platform.

© 2021 Optical Society of America

<http://dx.doi.org/10.1364/ao.XX.XXXXXX>

1. INTRODUCTION

When a nondegenerate quantum system makes a cyclic evolution in the Hilbert space, it will pick up a phase, which, in general, is contributed by both the dynamical and geometric effects. The dynamical part is the time integral of the energy, while the geometric one depends upon the area enclosed by the loop that the quantum state traverses in the Hilbert space. This effect, discovered by Berry in cyclic and adiabatic evolutions [1], has been generalized to nonadiabatic [2] and nondegenerate [3] cases. If a system has degenerate energy levels, the cyclic evolution of the corresponding degenerate subspaces will produce a matrix-valued quantum state transformation that is path-dependent and referred to as non-Abelian geometric phase or holonomy [3]. The Berry phase and holonomy depend upon the global geometry of the associated loops and have intrinsic resistance to certain kinds of small errors, suggesting quantum gates based on geometric operations have practical advantages as compared to dynamical gates [4–7]. In particular, it was shown that all of the elementary one- and two-qubit gates needed for accomplishing any quantum computation task could be achieved with Berry phase and holonomic transformations, offering a possibility for

implementations of geometric quantum computation [8, 9].

The conditional Berry phase was first observed in nuclear magnetic resonance systems [10]. However, the relatively long operation time associated with an adiabatic evolution represents an unfavorable condition for the implementation of geometric quantum computation with such controlled phase gates. As such, geometric effects without the adiabatic restriction are highly desirable for the implementation of quantum logic gates that are robust against noises [11–16]. So far, nonadiabatic geometric controlled-phase gates have been realized in ion traps [17–20] and superconducting circuits [21–23]. On the other hand, Sjöqvist *et al.* have proposed an approach for realizing a universal set of elementary gates based on nonadiabatic holonomies [24], whose robustness against noises has been analyzed [25, 26]. Following this approach, a universal gate set involving two non-commutable single-qubit gates and a two-qubit controlled-Not (CNOT) gate have been experimentally realized with nuclear magnetic resonance [27] and solid-state spins [28, 29]. Several groups have demonstrated holonomic single-qubit gates in superconducting circuits [30–33], which represent a promising platform for quantum computation [34]. Recently, Egger *et al.*

reported a holonomic operation for producing entangled states in a superconducting circuit [35]. However, a non-Abelian geometric entangling gate necessary for constructing a universal holonomic gate set has not been implemented in such scalable systems. More recently, Han et al. reported a universal set of time-optimal geometric gates with superconducting qubits [36], where single-qubit gates were realized using non-Abelian geometric phase, but the two-qubit gate was based on Abelian geometric phase.

In this paper, we propose and experimentally demonstrate a scheme for realizing non-adiabatic, non-Abelian geometric CNOT gate for two qubits, one acting as the control qubit and the other as the target qubit. The two qubits are strongly coupled to a resonator, so that the energy levels of the target qubit depend on the state of the control qubit. This conditional energy-level shift enables the target qubit to be resonantly driven by classical fields, conditional on the state of the control qubit. With suitable setting of the parameters, these classical fields can drive the degenerate subspace spanned by the two basis states of the target qubit to undergo a conditional cyclic evolution, realizing a CNOT gate between these two qubits. We realize this holonomic gate in a superconducting multi-qubit processor, where any two qubits can be selectively coupled to a common resonator but effectively decoupled from other qubits through frequency tuning. This flexibility enables direct implementation of holonomic gates between any pair of qubits on the chip, without the restriction of nearest-neighbor couplings. The measured process fidelity for the CNOT gate is above 0.9. With further improvements in the device design and fabrication, as confirmed by our numerical simulations, the gate fidelity can be significantly increased. Our scheme is applicable to other spin-boson systems, such as cavity QED and ion traps [37].

2. THEORETICAL MODEL

The system under consideration is composed of two qubits coupled to a resonator. Each qubit has three basis states, as shown in Fig. 1a, with $|g\rangle$ and $|f\rangle$ serving as two logic states of a qubit, and $|e\rangle$, lying between $|g\rangle$ and $|f\rangle$, used as an auxiliary state for realizing the controlled logic operation. For simplicity, we will refer to the qubits as qubits. As will be shown, the control qubit (Q_1) remains in its computational space, while the target qubit (Q_2) has a probability of being populated in the auxiliary level $|e\rangle$ during the gate operation. The transition $|g\rangle \leftrightarrow |e\rangle$ of each qubit resonantly interacts with the resonator, while $|f\rangle$ state is effectively decoupled from the resonator. In the interaction picture, the Hamiltonian describing the qubit-resonator interaction is given by

$$H_{\text{int}} = \hbar \sum_{j=1}^2 \lambda_j \left(a |e_j\rangle \langle g_j| + a^\dagger |g_j\rangle \langle e_j| \right), \quad (1)$$

where a and a^\dagger are the photonic annihilation and creation operators for the resonator, λ_j is the coupling strength between the j th qubit and the resonator with angular frequency ω_r . We here have set the energy of the ground state $|g\rangle$ for each qubit to be 0. To realize the CNOT gate, the transition $|g_2\rangle \leftrightarrow |e_2\rangle$ of Q_2 is driven by a classical field with angular frequency $(\omega_r - \lambda_2)$, and $|e_2\rangle \leftrightarrow |f_2\rangle$ is driven by a classical field with angular frequency $(\omega_{f,2} - \omega_r + \lambda_2)$, where $\hbar\omega_{f,2}$ is the energy of Q_2 's state $|f_2\rangle$ (Fig. 1a). The interaction between the second qubit

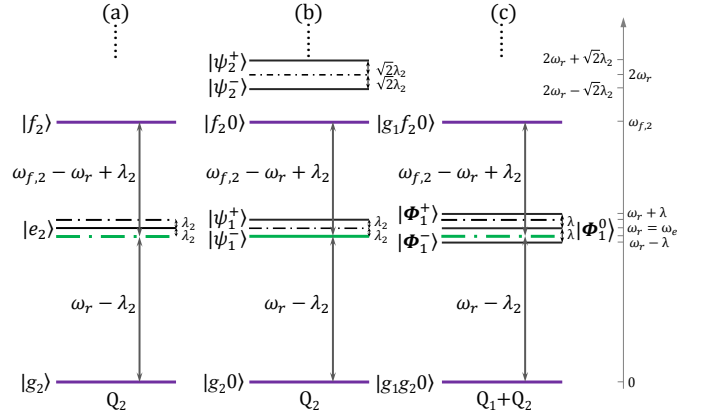


Fig. 1. Energy level configuration and excitation scheme for the two-qubit CNOT gate. The control and target qubits are denoted as Q_1 and Q_2 , respectively. (a) Bare energy levels of Q_2 and frequencies of the drives. The quantum information of each qubit is encoded in the states $|g\rangle$ and $|f\rangle$, with the auxiliary state $|e\rangle$ used for realizing the controlled-NOT gate. The transitions $|g_2\rangle \leftrightarrow |e_2\rangle$ and $|e_2\rangle \leftrightarrow |f_2\rangle$ of Q_2 are driven by classical fields of angular frequencies $(\omega_r - \lambda_2)$ and $(\omega_{f,2} - \omega_r + \lambda_2)$, respectively. Here ω_r is the angular frequency of the resonator that is strongly coupled to $|g_2\rangle \leftrightarrow |e_2\rangle$ with the coupling strength λ_2 , and $\hbar\omega_{f,2}$ is the energy spacing between $|f_2\rangle$ and $|g_2\rangle$. (b) Dressed states and energy levels with Q_1 initially in $|f_1\rangle$. When being initially in $|f_1\rangle$, Q_1 is effectively decoupled from the resonator due to the large detuning. The strong coupling between Q_2 and the resonator results in dressed states $|\psi_n^\pm\rangle$, whose energy levels are nonlinearly dependent on the coupling strength. The two driving fields are on resonance with the transitions $|g_2 0\rangle \leftrightarrow |\psi_1^-\rangle$ and $|\psi_1^-\rangle \leftrightarrow |f_2 0\rangle$, respectively, but highly detuned from other transitions. (c) Dressed states and energy levels with Q_1 initially in $|g_1\rangle$. If initially in $|g_1\rangle$, Q_1 , together with Q_2 , is strongly coupled to the resonator, resulting in three dressed states $|\Phi_1^\pm\rangle$ and $|\Phi_1^0\rangle$ in the single-excitation subspace. The driving fields are highly detuned from transitions of $|g_1 g_2 0\rangle$ and $|g_1 f_2 0\rangle$ to these dressed states.

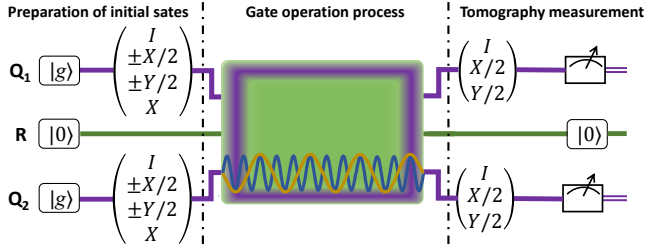


Fig. 2. Pulse sequence. Before the gate operation, both qubits are initialized to their ground state at the corresponding idle frequencies, where single-qubit rotations are performed to prepare them in a product state. Then a Z pulse is applied to Q_1 , tuning $|g_1\rangle \leftrightarrow |e_1\rangle$ close to the resonator's frequency; Q_2 is subjected to a Z pulse, which brings $|g_2\rangle \leftrightarrow |e_2\rangle$ to the resonator's frequency, and a driving pulse involving two frequency components respectively on resonance with the transitions $|g_20\rangle \leftrightarrow |\psi_1^-\rangle$ and $|\psi_1^-\rangle \leftrightarrow |f_20\rangle$. After the CNOT gate, realized with these pulses, both qubits are tuned back to their idle frequencies for quantum state tomography.

and the driving fields is described by

$$H_{\text{dr}} = \hbar \left[\Omega_{ge} e^{i\lambda_2 t} |e_2\rangle \langle g_2| - \Omega_{ef} e^{-i\lambda_2 t} |f_2\rangle \langle e_2| \right] + h.c. \quad (2)$$

where Ω_{ge} and Ω_{ef} denote the Rabi frequencies of the two fields driving $|g_2\rangle \leftrightarrow |e_2\rangle$ and $|e_2\rangle \leftrightarrow |f_2\rangle$, respectively. We here have assumed that the phases of the fields driving the transitions $|g\rangle \leftrightarrow |e\rangle$ and $|e\rangle \leftrightarrow |f\rangle$ are 0 and π , respectively.

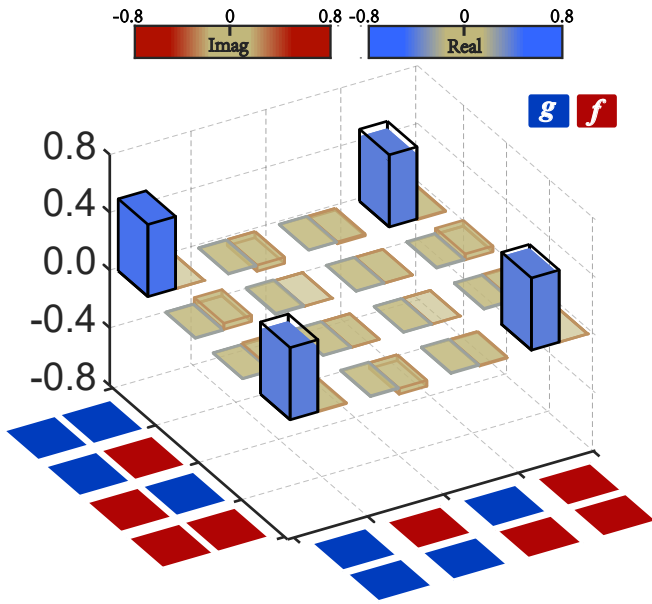


Fig. 3. Measured density matrix of the output state with the input state $(|g_1g_2\rangle + |f_1g_2\rangle) / \sqrt{2}$. Each matrix element is characterized by two colorbars, one for the real part and the other for the imaginary part. The black wire frames denote the matrix elements of the ideal output states.

The strong couplings between the qubits and the resonator produce dressed states, whose energy levels depend on the total excitation number as well as on the number of qubits being initially populated in $|g\rangle$. When the control qubit is in the state

$|f_1\rangle$, it does not interact with the resonator, and the coupling between the target qubit and the resonator is described by the Jaynes-Cummings model, whose eigenstates are given by

$$|\psi_0\rangle = |g_20\rangle, \quad (3)$$

$$|\psi_n^\pm\rangle = \frac{1}{\sqrt{2}} (|e_2(n-1)\rangle \pm |g_2n\rangle), \quad n \geq 1. \quad (4)$$

Here the second symbol in each ket denotes the photon number in the resonator. The eigenenergies of the dressed states $|\psi_n^\pm\rangle$ are $\hbar(n\omega_r \pm \sqrt{n}\lambda_2)$. We here consider the case that the resonator is initially in the vacuum state $|0\rangle$. Consequently, the classical fields resonantly couple the states $|g_20\rangle$ and $|f_20\rangle$ to the single-excitation dressed state $|\psi_1^-\rangle$, respectively, as sketched in Fig. 1b. We suppose that Ω_{ge} and Ω_{ef} are much smaller than λ_2 , so that the classical fields cannot drive the transitions from $|\psi_1^-\rangle$ to $|\psi_2^\pm\rangle$ due to the large detunings. However, these off-resonant couplings shift the energy levels of $|\psi_1^-\rangle$ by $-2\hbar\delta_1$, with $\delta_1 = 2\Omega_{ge}^2/\lambda_2$ (see Supplemental Material). Furthermore, off-resonant coupling to $|h_1\rangle |g_20\rangle$ and $|e_1\rangle |\psi_2^\pm\rangle$ shifts the energy level of $|f_1\rangle |\psi_1^\pm\rangle$ by an amount of $-\hbar\delta_2$, where $\delta_2 = 9\lambda_1^2/4\alpha_1$ (see Supplemental Material), and $|h_1\rangle$ is the fourth level of Q_1 and α_1 is its anharmonicity ($\alpha_j = 2\omega_{e,j} - \omega_{f,j}$, $j = 1, 2$). To compensate for these shifts, the angular frequency of the field driving $|g_2\rangle \leftrightarrow |e_2\rangle$ should be set to $\omega_{d,1} = \omega_r - \lambda_2 - \delta_1 - \delta_2$, while that of the field driving $|e_2\rangle \leftrightarrow |f_2\rangle$ should be set to $\omega_{d,2} = \omega_{f,2} - \omega_r + \lambda_2 + \delta_1 + \delta_2$. With this setting and performing the transformation $\exp(iH_{\text{int}}t/\hbar)$, the system dynamics associated with Q_1 's state $|f_1\rangle$ can be described by the effective Hamiltonian

$$H_{\text{eff}} = \hbar\Omega \left[\cos \frac{\phi}{2} |g_20\rangle \langle \psi_1^-| + \sin \frac{\phi}{2} |f_20\rangle \langle \psi_1^-| \right] |f_1\rangle \langle f_1| + h.c., \quad (5)$$

where

$$\Omega = \sqrt{\Omega_{ge}^2 + \Omega_{ef}^2} / \sqrt{2}, \quad (6)$$

$$\tan \frac{\phi}{2} = \Omega_{ef} / \Omega_{ge}. \quad (7)$$

When Q_1 is initially in the state $|g_1\rangle$, it is also strongly coupled to the resonator, and there are three dressed states in the single-excitation subspace:

$$|\Phi_1^0\rangle = (-\sin \theta |e_1g_20\rangle + \cos \theta |g_1e_20\rangle), \quad (8)$$

$$|\Phi_1^\pm\rangle = \frac{1}{\sqrt{2}} [(\cos \theta |e_1g_20\rangle + \sin \theta |g_1e_20\rangle) \pm |g_1g_21\rangle], \quad (9)$$

where $\tan \theta = \lambda_2/\lambda_1$. The corresponding eigenenergies are $\hbar\omega_e$ and $\hbar(\omega_e \pm \sqrt{\lambda_1^2 + \lambda_2^2})$, as shown in Fig. 1c. When $(\sqrt{\lambda_1^2 + \lambda_2^2} - \lambda_2)$ is much larger than Ω_{ge} and Ω_{ef} , the qubits cannot make any transition between each of these single-excitation dressed states and the state $|g_1g_20\rangle$ or $|g_1f_20\rangle$ as each of these transitions is highly detuned from the driving fields. As a consequence, Q_2 is not affected by the driving fields when Q_1 is initially in the state $|g_1\rangle$. Therefore, the system dynamics is described by the effective Hamiltonian of Eq. (5). The evolution of the initial basis states $|c_1d_20\rangle$ ($c, d = g, f$) are given by

$$|\psi_{cd}(t)\rangle = \exp\left(-i \int_0^t H_{\text{eff}} dt / \hbar\right) |c_1d_20\rangle. \quad (10)$$

When Ω_{ef}/Ω_{ge} remains unchanged during the interaction, the evolution satisfies the parallel-transport condition

$\langle \psi_{cd}(t) | H_{\text{eff}} | \psi_{c'd'}(t) \rangle = 0$, and hence is purely geometric. If the Rabi frequencies of the driving fields and the interaction time are appropriately chosen so that $\int_0^T \Omega dt = \pi$, the degenerate qubit subspace undergoes a cyclic evolution. Consequently, the qubits return to the computational space $\{|g_1g_2\rangle, |g_1f_2\rangle, |f_1g_2\rangle, |f_1f_2\rangle\}$ with the resonator left in the vacuum state $|0\rangle$ after the time T . With this setting, the evolution operator of the qubits in the computational basis is

$$U = \begin{pmatrix} 1 & 0 & 0 & 0 \\ 0 & 1 & 0 & 0 \\ 0 & 0 & -\cos \phi & \sin \phi \\ 0 & 0 & \sin \phi & \cos \phi \end{pmatrix}, \quad (11)$$

which is a non-Abelian holonomy. For $\phi = \pi/2$, i.e., $\Omega_{ge} = \Omega_{ef}$, this corresponds to a CNOT gate, which flips the state of the target qubit conditional on the control qubit being in the state $|f_1\rangle$.

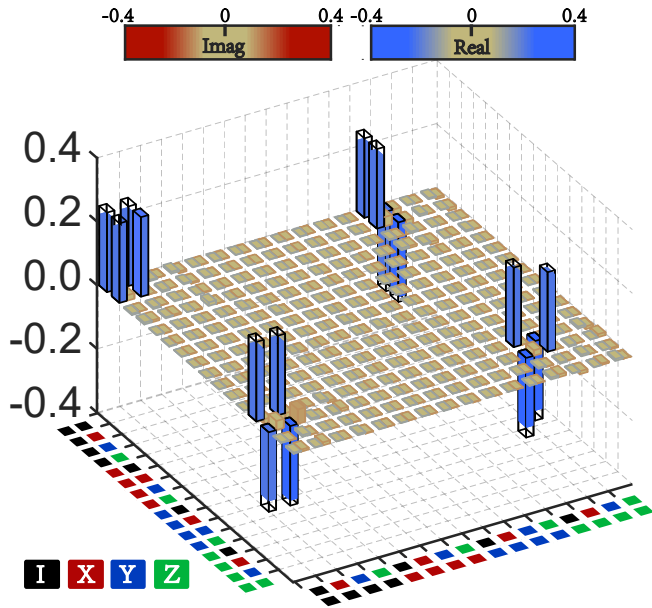


Fig. 4. Measured process matrix for the realized CNOT gate. The process matrix is measured by preparing a set of 36 distinct input product states in the computational basis $\{|g_1g_2\rangle, |g_1f_2\rangle, |f_1g_2\rangle, |f_1f_2\rangle\}$ and reconstructing the density matrices for these states and for the output states produced by the CNOT gate. The $|e\rangle$ -state populations of Q_1 and Q_2 , averaged over the 36 output states, are 2.2% and 2.8%, respectively.

3. EXPERIMENTAL IMPLEMENTATION

The experiment is performed in a superconducting circuit involving five frequency-tunable qubits, labeled from Q_1 to Q_5 , coupled to a resonator with a fixed frequency $\omega_r/2\pi = 5.584$ GHz [21, 38, 39]. In our experiment, Q_1 and Q_2 , whose anharmonicities are $2\pi \times 242$ MHz and $2\pi \times 249$ MHz, are used as the control and target qubits, respectively. The on-resonance coupling strengths of the g - e transitions of Q_1 and Q_2 to the resonator are respectively $\lambda_1 = 2\pi \times 20.8$ MHz and $\lambda_2 = 2\pi \times 19.9$ MHz. The energy relaxation time T_1 and pure Gaussian dephasing time T_2^* for the basis state $|f\rangle$ of Q_1 (Q_2) are 13.0 (10.7) μ s

and 2.1 (1.5) μ s, while those for the intermediate state $|e\rangle$ are 23.9 (15.9) μ s and 2.7 (2.1) μ s, respectively. The other qubits are on far off-resonance with the resonator so that their interactions with the resonator are effectively switched off throughout the gate operation. We note that during the gate operation, the two qubits have a probability of being populated in $|f_1e_2\rangle$, which is significantly coupled to $|e_1f_2\rangle$ via virtual photon exchange as the two qubits almost have the same anharmonicity $\alpha \simeq 2\pi \times 240$ MHz. To suppress this coupling, Q_1 should be detuned from Q_2 by an amount much larger than $\lambda_1\lambda_2/\alpha$. This detuning slightly changes the energy level configuration of the dressed states associated with Q_1 's initial state $|g_1\rangle$, but does not affect the gate dynamics.

As shown in Fig. 2, the experiment starts with the initialization of Q_1 and Q_2 to the ground state $|g\rangle$ at their idle frequencies 5.47 GHz and 5.43 GHz, respectively, which is followed by the preparation of each qubit in one of the six states $\{|g\rangle, (|g\rangle - i|f\rangle)/\sqrt{2}, (|g\rangle + i|f\rangle)/\sqrt{2}, (|g\rangle + |f\rangle)/\sqrt{2}, (|g\rangle - |f\rangle)/\sqrt{2}, |f\rangle\}$. Except $|g\rangle$, each of the other single-qubit states is produced by a g - e $\pi/2$ - or π -pulse followed by a e - f π -pulse. After these effective single-qubit rotations, these two qubits are prepared in a product state. We then apply square Z pulses to both qubits, tuning their $|g\rangle \leftrightarrow |e\rangle$ transition frequencies to 5.58 GHz and 5.584 GHz and thus switching on their interactions with the resonator. Accompanying these Z pulses, a driving pulse composed of two components with frequencies of 5.565 GHz and 5.369 GHz is applied to Q_2 , resonantly connecting the computational states $|g_20\rangle$ and $|f_20\rangle$ to the dressed state $|\psi_1^-\rangle$. The Rabi frequencies of these driving fields are $\Omega_{ge} = \Omega_{ef} = 2\pi \times 2.2$ MHz. Since the resonator is initially in the vacuum state, the system dynamics is governed by the effective Hamiltonian (5) and the time evolution given by Eq. (10). After a duration of $\tau = 205$ ns, the CNOT gate is realized.

One of the most important features of the CNOT gate is that it can convert a two-qubit product state into an entangled state. In particular, when the control qubit is initially in the superposition state $(|g_1\rangle + |f_1\rangle)/\sqrt{2}$ and the target state in $|g_2\rangle$, they will evolve to the maximally entangled state $(|g_1g_2\rangle + |f_1f_2\rangle)/\sqrt{2}$ after this gate. We measure this output state by quantum state tomography. This is realized by subsequently biasing each of the two qubits back to its idle frequency right after the gate operation, applying an e - f π -pulse to each qubit, and measuring its state along one of the three orthogonal (X, Y, and Z) axes of the corresponding Bloch sphere with respect to the basis $\{|g\rangle, |e\rangle\}$. The Z measurement is directly realized by state readout, while the X (Y) measurement realized by the combination of a g - e $\pi/2$ -pulse and state readout. The reconstructed output two-qubit density matrix is displayed in Fig. 3, which has a fidelity of 0.935 ± 0.016 to the ideal maximally entangled state, and a concurrence of 0.888 ± 0.029 .

To fully characterize the performance of the implemented CNOT gate, we prepare a full set of 36 distinct two-qubit input states before the two-qubit gates, and measure these states and the corresponding output states. With these measured results, the process matrix for the gate operation is reconstructed. The measured process matrix, χ_{meas} , is presented in Fig. 4. The gate fidelity, defined as $F = \text{tr}(\chi_{\text{id}}\chi_{\text{meas}})$, is 0.905 ± 0.008 , where χ_{id} is the ideal process matrix. The measured fidelity is in well agreement with the numerical simulation based on the Lindblad master equation, which yields a fidelity of 0.908. One of the error sources is the transitions from $|g_1g_20\rangle$ and $|g_1f_20\rangle$ to $|\Phi_1^0\rangle$ and $|\Phi_1^\pm\rangle$ and the transition from $|\psi_1^-\rangle$ to $|\psi_2^-\rangle$ induced by the

drive, which cause quantum information leakage to the noncomputational space. Such a leakage error can be mitigated through the improvement of the qubit's nonlinearity or by balancing the drive amplitude and the gate operation time provided the qubits' coherence is bettered, which allows the gate fidelity to be increased by about 6.5% (see Supplemental Material). On the other hand, the qubits' energy relaxation and their dephasings contribute about 1.8% and 1.6% of the error, respectively. Our further numerical simulations show that the CNOT gate with a fidelity above 99% can be obtained with sufficiently large qubit's nonlinearity α_j and qubit-resonator coupling strength λ_j . For instance, with the parameters $\lambda_j/2\pi = 110$ MHz, $\alpha_j/2\pi = -3.69$ GHz [40, 41], $\Omega_{ge}/2\pi = \Omega_{ef}/2\pi = 5.9$ MHz, $T_1 = 60$ μ s, and $T_{2,j}^* = 86$ μ s, we find a CNOT gate with the operation time about 87 ns and the fidelity of 0.991, which is at the surface code threshold for fault tolerance [42–44]. We note this gate is robust against the frequency fluctuations of the driving fields. Suppose that the angular frequencies of these drives deviate from the desired values by an amount of $\delta\omega = 2\pi \times 100$ kHz. The infidelity incurred by this deviation is about $[\pi(\delta\omega)^2 / (8\Omega_{ge/ef}^2)]^2 \simeq 0.1\%$.

4. CONCLUSION

In conclusion, we have proposed and demonstrated a scheme for implementing a non-Abelian geometric gate between two superconducting qubits, whose ground and second excited states act as the computational basis states. The conditional dynamics is realized by resonantly driving the transitions between the basis states of the target qubit to the single-excitation dressed states formed by this qubit and the resonator. This entangling gate, together with the previously demonstrated non-Abelian geometric single-qubit gates [30–33], constitutes a universal set of holonomic gates for realizing quantum computation with superconducting qubits. The method can be directly applied to other systems composed of qubits coupled to a bosonic mode, including cavity QED and ion traps.

Funding. National Natural Science Foundation of China (Grant No. 11674060, No. 11874114, No. 11875108, No. 11934018, No. 11904393, and No. 92065114), Strategic Priority Research Program of Chinese Academy of Sciences (Grant No. XDB28000000), and Beijing Natural Science Foundation (Grant No. Z200009).

Acknowledgment. We thank Haohua Wang at Zhejiang University for technical support.

Disclosures. The authors declare no conflicts of interest.

Contributions. S.-B.Z. conceived the experiment. K.X., W. N., and Z.-B.Y. performed the experiment and analyzed the data with the assistance of X.-J.H. and P.-R.H. H.L. and D.Z. provided the devices used for the experiment. S.-B.Z., Z.-B.Y., K.X., and H.F. wrote the manuscript with feedbacks from all authors. The experiment was performed at Fuzhou University.

REFERENCES

- M. V. Berry, "Quantal phase-factors accompanying adiabatic changes," *Proc. R. Soc. Lond. A* **392**, 45 (1984).
- Y. Aharonov and A. Anandan, "Phase change during a cyclic quantum evolution," *Phys. Rev. Lett.* **58**, 1593 (1987).
- F. Wilczek and A. Zee, "Appearance of gauge structure in simple dynamical systems," *Phys. Rev. Lett.* **52**, 2111 (1984).
- G. D. Chiara and G. M. Palma, "Berry phase for a spin 1/2 particle in a classical fluctuating field," *Phys. Rev. Lett.* **91**, 090404 (2003).
- S. Filipp, J. Klepp, Y. Hasegawa, C. Plonka-Spehr, U. Schmidt, P. Geltenbort, and H. Rauch, "Experimental demonstration of the stability of Berry's phase for a spin-1/2 particle," *Phys. Rev. Lett.* **102**, 030404 (2009).
- A. Carollo, I. Fuentes-Guridi, M. F. Santos, and V. Vedral, "Geometric phase in open systems," *Phys. Rev. Lett.* **90**, 160402 (2003).
- S.-B. Zheng, "Geometric phase for a driven quantum field subject to decoherence," *Phys. Rev. A* **91**, 052117 (2015).
- P. Zanardi and M. Rasetti, "Holonomic quantum computation," *Phys. Lett. A* **264**, 94 (1999).
- J. Pachos, P. Zanardi, and M. Rasetti, "Non-Abelian Berry connections for quantum computation," *Phys. Rev. A* **61**, 010305(R) (2000).
- J. A. Jones, V. Vedral, A. Ekert, and G. Castagnoli, "Geometric quantum computation with NMR," *Nature (London)* **403**, 869 (2000).
- X.-B. Wang and M. Keiji, "Nonadiabatic conditional geometric phase shift with NMR," *Phys. Rev. Lett.* **87**, 097901 (2001).
- S.-L. Zhu and Z.-D. Wang, "Implementation of universal quantum gates based on nonadiabatic geometric phases," *Phys. Rev. Lett.* **89**, 097902 (2002).
- A. Nazir, T. Spiller, and W. J. Munro, "Decoherence of geometric phase gates," *Phys. Rev. A* **65**, 042303 (2002).
- A. Blais and A.-M. S. Tremblay, "Effect of noise on geometric logic gates for quantum computation," *Phys. Rev. A* **67**, 012308 (2003).
- J. Zhang, S. J. Devitt, J. Q. You, and F. Nori, "Holonomic surface codes for fault-tolerant quantum computation," *Phys. Rev. A* **97**, 022335 (2018).
- Y.-H. Chen, W. Qin, R. Stassi, X. Wang, and F. Nori, "Generation of Fock-State Superpositions and binomial-code holonomic gates via dressed intermediate states in the ultrastrong light-matter coupling Regime," arXiv:2012.06090.
- D. Leibfried, B. DeMarco, V. Meyer, D. Lucas, M. Barrett, J. Britton, W. M. Itano, B. Jelenković, C. Langer, T. Rosenband, and D. J. Wineland, "Experimental demonstration of a robust, high-fidelity geometric two ion-qubit phase gate," *Nature (London)* **422**, 412 (2003).
- J. Benhelm, G. Kirchmair, C. F. Roos, and R. Blatt, "Towards fault-tolerant quantum computing with trapped ions," *Nat. Phys.* **4**, 463 (2008).
- C. J. Ballance, T. P. Harty, N. M. Linke, M. A. Sepiol, and D. M. Lucas, "High-fidelity quantum logic gates using trapped-ion hyperfine qubits," *Phys. Rev. Lett.* **117**, 060504 (2016).
- J. P. Gaebler, T. R. Tan, Y. Lin, Y. Wan, R. Bowler, A. C. Keith, S. Glancy, K. Coakley, E. Knill, D. Leibfried, and D. J. Wineland, "High-fidelity universal gate set for ${}^9\text{Be}^+$ ion qubits," *Phys. Rev. Lett.* **117**, 060505 (2016).
- C. Song, S.-B. Zheng, P. Zhang, K. Xu, L. Zhang, Q. Guo, W. Liu, D. Xu, H. Deng, K. Huang, D. Zheng, X. Zhu, H. Wang, "Continuous-variable geometric phase and its manipulation for quantum computation in a superconducting circuit," *Nat. Commun.* **8**, 1061 (2017).
- Y. Xu, Z. Hua, T. Chen, X. Pan, X. Li, J. Han, W. Cai, Y. Ma, H. Wang, Y. P. Song, Z.-Y. Xue, and L. Sun, "Experimental implementation of universal nonadiabatic geometric quantum gates in a superconducting circuit," *Phys. Rev. Lett.* **124**, 230503 (2020).
- Y. Xu, Y. Ma, W. Cai, X. Mu, W. Dai, W. Wang, L. Hu, X. Li, J. Han, H. Wang, Y. P. Song, Z.-B. Yang, S.-B. Zheng, and L. Sun, "Demonstration of Controlled-Phase Gates Between Two Error-Correctable Photonic Qubits," *Phys. Rev. Lett.* **124**, 120501 (2020).
- E. Sjöqvist, D. M. Tong, L. M. Andersson, B. Hessmo, M. Johansson, and K. Singh, "Nonadiabatic holonomic quantum computation," *N. J. Phys.* **14**, 103035 (2012).
- M. Johansson, E. Sjöqvist, L. M. Andersson, M. Ericsson, B. Hessmo, K. Singh, and D. M. Tong, "Robustness of non-adiabatic holonomic gates," *Phys. Rev. A* **86**, 062322 (2012).
- S.-B. Zheng, C.-P. Yang, and F. Nori, "Comparison of the sensitivity to systematic errors between nonadiabatic non-Abelian geometric gates and their dynamical counterparts," *Phys. Rev. A* **93**, 032313 (2016).
- G. Feng, G. Xu, and G. Long, "Experimental realization of nonadiabatic holonomic quantum computation," *Phys. Rev. Lett.* **110**, 190501 (2013).
- C. Zu, W.-B. Wang, L. He, W.-G. Zhang, C.-Y. Dai, F. Wang, L.-M. Duan, "Experimental realization of universal geometric quantum gates with

- solid-state spins," *Nature* **514**, 72 (2014).
29. S. Arroyo-Camejo, A. Lazariév, S. W. Hell, and G. Balasubramanian, "Room temperature high-fidelity holonomic single-qubit gate on a solid-state spin," *Nat. Commun.* **5**, 4870 (2014).
 30. A. A. Abdumalikov Jr, J. M. Fink, K. Juliusson, M. Pechal, S. Berger, A. Wallraff, and S. Filipp, "Experimental realization of non-Abelian nonadiabatic geometric gates," *Nature (London)* **496**, 482 (2013).
 31. Y. Xu, W. Cai, Y. Ma, X. Mu, L. Hu, Tao Chen, H. Wang, Y.-P. Song, Z.-Y. Xue, Z.-Q. Yin, L. Sun, "Single-loop realization of arbitrary non-adiabatic holonomic single-qubit quantum gates in a superconducting circuit," *Phys. Rev. Lett.* **121**, 110501 (2018).
 32. T. Yan, B.-J. Liu, K. Xu, C. Song, S. Liu, Z. Zhang, H. Deng, Z. Yan, H. Rong, K. Huang, M.-H. Yung, Y. Chen, and D. Yu, "Experimental realization of nonadiabatic shortcut to non-Abelian geometric gates," *Phys. Rev. Lett.* **122**, 080501 (2019).
 33. Z. Zhang, P.-Z. Zhao, T. Wang, L. Xiang, Z. Jia, P. Duan, D.-M. Tong, Y. Yin, and G. Guo, "Single-shot realization of nonadiabatic holonomic gates with a superconducting Xmon qutrit," *New J. Phys.* **21**, 073024 (2019).
 34. J. Q. You and F. Nori, "Superconducting circuits and quantum information," *Phys. Today* **58**, 42 (2005).
 35. D. J. Egger, M. Ganzhorn, G. Salis, A. Fuhrer, P. Mueller, P. K. Barkoutsos, N. Moll, I. Tavernelli, and S. Filipp, "Entanglement generation in superconducting qubits using holonomic operations," *Phys. Rev. Applied* **11**, 014017 (2019).
 36. Z. Han, Y. Dong, B. Liu, X. Yang, S. Song, L. Qiu, D. Li, J. Chu, W. Zheng, J. Xu, T. Huang, Z. Wang, X. Yu, X. Tan, D. Lan, M.-H. Yung, and Y. Yu, "Experimental realization of universal time-optimal non-Abelian geometric gates," arXiv:2004.10364 (2020).
 37. I. Buluta, S. Ashhab, and F. Nori, "Natural and artificial atoms for quantum computation," *Reports on Progress in Physics* **74**, 104401 (2011).
 38. W. Ning, X.-J. Huang, P.-R. Han, H. Li, H. Deng, Z.-B. Yang, Z.-R. Zhong, Y. Xia, K. Xu, D. Zheng, and S.-B. Zheng, "Deterministic entanglement swapping in a superconducting circuit," *Phys. Rev. Lett.* **123**, 060502 (2019).
 39. Z.-B. Yang, P.-R. Han, X.-J. Huang, W. Ning, H. Li, K. Xu, D. Zheng, H. Fan, and S.-B. Zheng, "Experimental demonstration of entanglement-enabled universal quantum cloning in a circuit," *npj Quantum Inf* **7**, 44 (2021).
 40. M. A. Yurtalan, J. Shi, G. J. K. Flatt, and A. Lupascu, "Characterization of multi-level dynamics and decoherence in a high-anharmonicity capacitively shunted flux circuit," arxiv:2008.00593 (2020).
 41. J. Q. You, X. Hu, S. Ashhab and F. Nori, "Low-decoherence flux qubit," *Phys. Rev. B* **75**, 140515(R) (2007).
 42. A. G. Fowler, M. Mariantoni, J. M. Martinis, and A. N. Cleland, "Surface codes: Towards practical large-scale quantum computation," *Phys. Rev. A* **86**, 032324 (2012)
 43. R. Barends, J. Kelly, A. Megrant, A. Veitia, D. Sank, E. Jeffrey, T. C. White, J. Mutus, A. G. Fowler, B. Campbell, Y. Chen, Z. Chen, B. Chiaro, A. Dunsworth, C. Neill, P. O'Malley, P. Roushan, A. Vainsencher, J. Wenner, A. N. Korotkov, A. N. Cleland, and J. M. Martinis, "Superconducting quantum circuits at the surface code threshold for fault tolerance," *Nature (London)* **508**, 500 (2014).
 44. R. Barends, A. G. Fowler, A. Megrant, E. Jeffrey, T. C. White, D. Sank, J. Y. Mutus, B. Campbell, Yu Chen, Z. Chen, B. Chiaro, A. Dunsworth, I.-C. Hoi, C. Neill, P. J. J. O'Malley, C. Quintana, P. Roushan, A. Vainsencher, J. Wenner, A. N. Cleland, and John M. Martinis, "State preservation by repetitive error detection in a superconducting quantum circuit," *Nature (London)* **519**, 66 (2015).

Supplementary material for “Demonstration of a non-Abelian geometric controlled-Not gate in a superconducting circuit”

1. DEVICE PARAMETERS

The device used in our experiment is similar to the ones reported in Refs. [1–3], it possesses five superconducting Xmon qutrits, whose basis states are denoted as $|g\rangle$, $|e\rangle$ and $|f\rangle$, as shown in Fig. 1 of the main text. These qutrits are capacitively connected to a bus resonator, whose rare frequency is measured as 5.584 GHz when all the qutrits are staying in the ground state $|g\rangle$ at their respective idle frequencies $\omega_j/2\pi$. Each qutrit’s frequency is flexibly adjusted and thus can be controlled to couple to the bus resonator in a dispersive or resonant manner, that induces virtual-photon-mediated [2, 4] or real-photon-mediated qubit-qubit coupling [5]. The coupling strength λ_j between each qutrit and the resonator through the $|g\rangle \leftrightarrow |e\rangle$ transition is measured through qutrit-resonator vacuum Rabi swap, while keeping the qutrit’s $|e\rangle \leftrightarrow |f\rangle$ transition decoupled as the qutrit’s anharmonicity α_j is much larger than λ_j . The device is kept inside a dilution refrigerator with a base temperature below 20 mK. We pick up two qutrits, which are labelled as Q_1 and Q_2 , for our implementation. The related parameters including the qutrit states’ coherence times and readout fidelities are characterized and listed in Table S1. As the computation information is encoded in $|g\rangle$ and $|f\rangle$ ($|e\rangle$ as the auxiliary state), we thus refer to the qutrits as qubits.

Table S1. Qubits characteristics.

	$\omega_j/2\pi$ (GHz)	$T_{1,j}^{(e)}$ (μ s)	$T_{2,j}^{*,(e)}$ (μ s)	$T_{2,j}^{\text{SE},(e)}$ (μ s)	$T_{1,j}^{(f)}$ (μ s)	$T_{2,j}^{*,(f)}$ (μ s)	$\alpha_j/2\pi$	$\lambda_j/2\pi$ (MHz)	$F_j^{(g)}$	$F_j^{(e)}$	$F_j^{(f)}$
Q_1	5.47	23.9	2.7	7.6	13.0	2.1	242	20.8	0.96	0.84	0.87
Q_2	5.34	15.9	2.1	8.5	10.7	1.5	249	19.9	0.98	0.87	0.89

The idle frequency of Q_j is $\omega_j/2\pi$, where single-qubit rotation pulses and tomographic pulses are applied. Here $T_{1,j}^{(k)}$, $T_{2,j}^{*,(k)}$ and $T_{2,j}^{\text{SE},(k)}$ ($k = e, f$) are respectively the energy relaxation time, the Ramsey dephasing time and the spin-echo dephasing time of Q_j ’s state $|k\rangle$ measured at the idle point. In addition, α_j is the qubit’s anharmonicity and λ_j is the coupling strength between Q_j and the bus resonator. The probability of detecting Q_j in state $|k\rangle$ when it is prepared in state $|k\rangle$ is $F_j^{(k)}$. The I - Q data to differentiate these basis states are plotted in Fig. S1.

2. STARK SHIFTS INDUCED BY THE OFF-RESONANT COUPLING

When the system is initially in $|f_1g_20\rangle$, the control qubit does not interact with the resonator, while the target qubit strongly couples with the resonator. Such a strong coupling produces the dressed states $|\psi_n^\pm\rangle$, with the corresponding eigenenergies $\hbar(n\omega_r \pm \sqrt{n}\lambda_2)$. The two microwave fields with the angular frequencies

$$\omega_{d1} = \omega_r - \lambda_2 \quad (\text{S1})$$

and

$$\omega_{d2} = \omega_f - \omega_r + \lambda_2 \quad (\text{S2})$$

resonantly drive the two transitions $|g_20\rangle \leftrightarrow |\psi_1^-\rangle$ and $|f_20\rangle \leftrightarrow |\psi_1^-\rangle$, respectively, as depicted in Fig. S2. As the Rabi frequencies Ω_{ge} and Ω_{ef} of the two driving fields are much smaller than the qubit-resonator coupling strength λ_2 , the two fields cannot drive the transition from $|\psi_1^-\rangle$

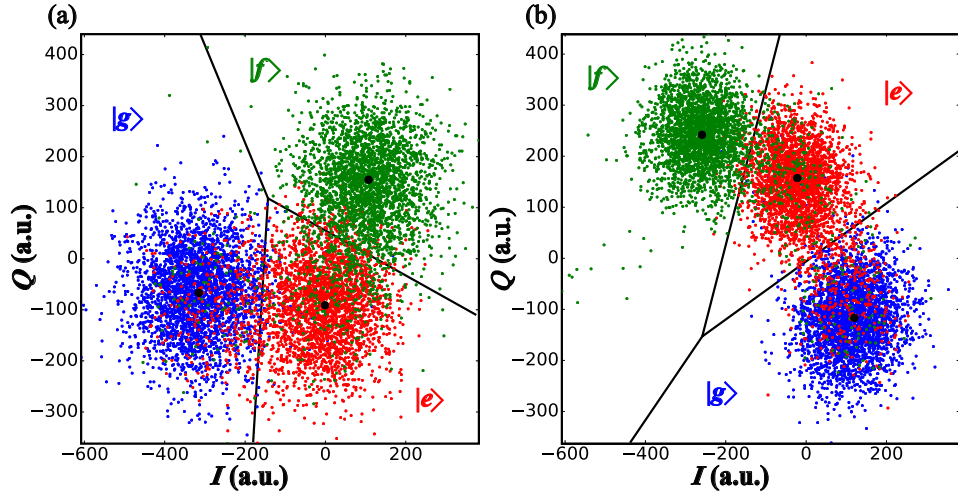


Fig. S1. The measured I - Q values when each qubit is prepared in $|g\rangle$ (blue), $|e\rangle$ (red) and $|f\rangle$ (green) state. (a) The I - Q data of the control qubit Q_1 . (b) The I - Q data of the target qubit Q_2 .

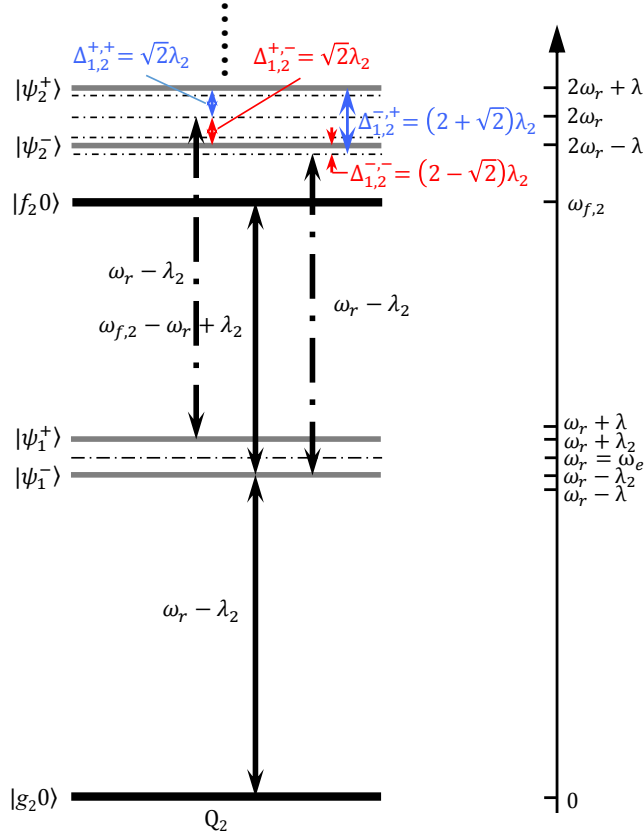


Fig. S2. Schematic diagram of the off-resonant couplings between the driving fields and the transitions $|\psi_1^\pm\rangle \leftrightarrow |\psi_2^\pm\rangle$. These lead to the energy shift $-2\hbar\Omega_{ge}^2/\lambda_2$, for $|\psi_1^- \rangle$.

to $|\psi_2^\pm\rangle$, whose energy gaps are $\hbar[\omega_r + (1 \pm \sqrt{2})\lambda_2]$, largely detuned from the two fields by the amount of

$$\Delta_{1,2,d1}^{-,\pm} = (2 \pm \sqrt{2})\lambda_2 \quad (\text{S3})$$

and

$$\Delta_{1,2,d2}^{-,\pm} = 2\omega_r - \omega_f \pm \sqrt{2}\lambda_2, \quad (\text{S4})$$

respectively. However, these off-resonant couplings shift the energy level of $|\psi_1^-\rangle$ by about $-\hbar\delta_1$, with $\delta_1 = \Omega_{ge}^2/(2 - \sqrt{2})\lambda_2 + \Omega_{ge}^2/(2 + \sqrt{2})\lambda_2 \equiv 2\Omega_{ge}^2/\lambda_2$. Besides, off-resonant couplings from $|f_1\rangle|\psi_1^-\rangle$ to $|h_1\rangle|g_20\rangle$ and $|e_1\rangle|\psi_2^\pm\rangle$ through the resonator photon also lead to energy shifts (see Fig. S3), which are

$$\hbar\delta_{2,1} = \hbar\left(\frac{\sqrt{3}\lambda_1}{\sqrt{2}}\right)^2/(2\alpha_1 - \lambda_2), \quad (\text{S5})$$

and

$$\hbar\delta_{2,2}^\pm = -\hbar\left[\frac{\sqrt{2}\lambda_1}{2}(1 \mp \sqrt{2})\right]^2/[\alpha_1 + (1 \pm \sqrt{2})\lambda_2], \quad (\text{S6})$$

respectively, three summing up to about $\hbar\delta_2 \simeq -9\lambda_1^2/4\alpha_1$.

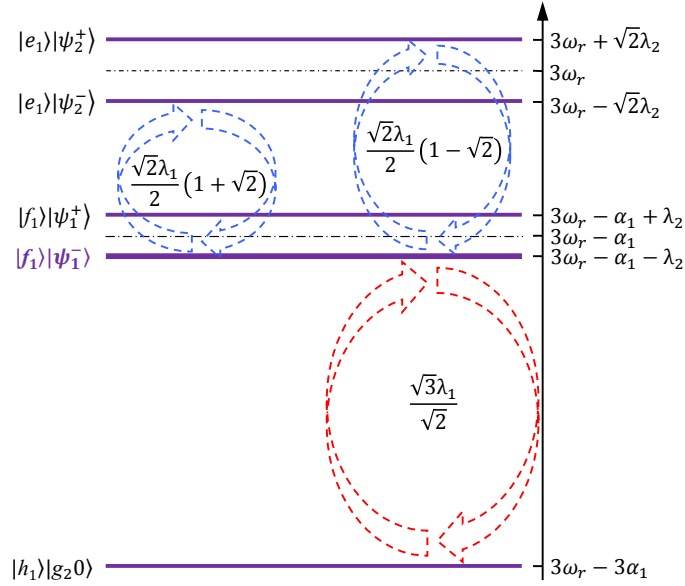


Fig. S3. Schematic diagram of the off-resonant couplings between the resonator photons and the transitions $|f_1\rangle|\psi_1^\pm\rangle \leftrightarrow |h_1\rangle|\psi_2^\pm\rangle$ and $|f_1\rangle|\psi_1^\pm\rangle \leftrightarrow |e_1\rangle|\psi_2^\pm\rangle$. The photon-induced Stark shifts for $|\psi_1^\pm\rangle$ are $\hbar\delta_2 \simeq -9\lambda_1^2/4\alpha_1$, approximately.

Note that the two fields also cannot drive the transition from $|\psi_1^+\rangle \leftrightarrow |\psi_2^\pm\rangle$, for which the energy gaps are $\hbar[\omega_r - (1 \mp \sqrt{2})\lambda_2]$, largely detuned from the two fields by

$$\Delta_{1,2,d1}^{+,\pm} = \pm\sqrt{2}\lambda_2 \quad (\text{S7})$$

and

$$\Delta_{1,2,d2}^{+,\pm} = 2\omega_r - \omega_f - (2 \mp \sqrt{2})\lambda_2, \quad (\text{S8})$$

respectively. Though the different off-resonant couplings lead to respective energy shifts to $|\psi_1^+\rangle$, such energy shifts are symmetric and thus neutralize to keep $|\psi_1^+\rangle$ almost constant. Note also that off-resonant couplings from $|f_1\rangle|\psi_1^+\rangle$ to $|h_1\rangle|g_20\rangle$ and $|e_1\rangle|\psi_2^\pm\rangle$ through the resonator photon lead to energy shifts, which are

$$\hbar\delta'_{2,1} = \hbar\left(\frac{\sqrt{3}\lambda_1}{\sqrt{2}}\right)^2/(2\alpha_1 + \lambda_2) \quad (\text{S9})$$

and

$$\hbar\delta_{2,2}^{\pm} = -\hbar\left[\frac{\sqrt{2}\lambda_1}{2}(1 \pm \sqrt{2})\right]^2 / [\alpha_1 - (1 \mp \sqrt{2})\lambda_2], \quad (\text{S10})$$

respectively, adding up to also about $\hbar\delta_2 \simeq -9\lambda_1^2/4\alpha_1$.

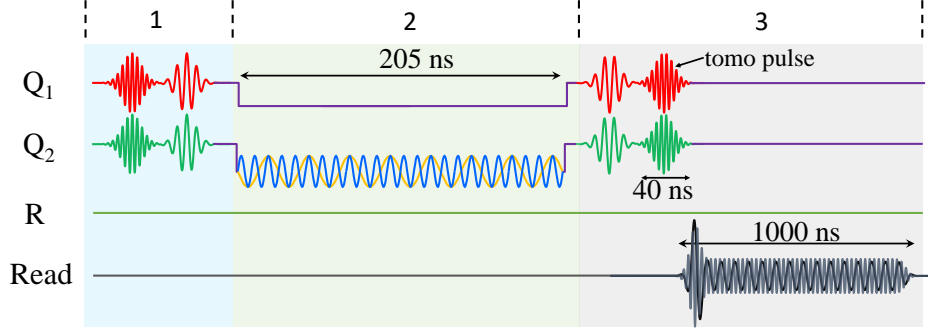


Fig. S4. The experimental sequence, which consists of three steps: initial state preparation, gate operation and quantum state tomography. The initial state is created by applying microwave pulses with a Gaussian envelop at the idle points. Then, in the second step, qubit frequencies are tuned by rectangular waves to be near (Q_1) or on resonance (Q_2) with the resonator. Q_2 is subjected to a two-tone microwave pulse with a flattop envelop during the interaction time which lasts about 205 ns. In the third step, tomographic operations are executed before the two-qubit joint readout.

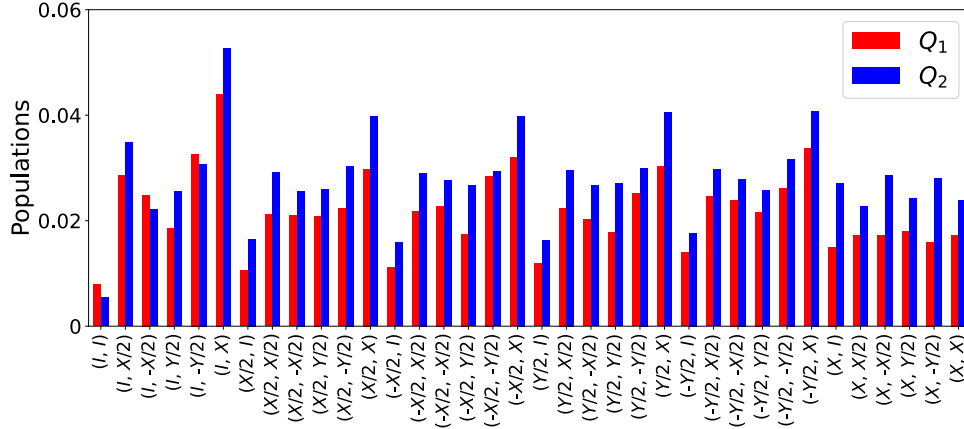


Fig. S5. The probabilities of leaking to the $|e\rangle$ state for each qubit. The probabilities are measured after the gate sequence is finished for all 36 input states. The labels in the x -axis represent the single qubit rotations used to prepare the initial states.

3. EXPERIMENTAL SEQUENCE OF THE HOLONOMIC GATE

Figure S4 shows the experimental sequence, which is divide into three steps. Firstly, two successive microwave pulses are imposed on each qubit at their idle points to prepare the initial state. The first pulse with the frequency of $\omega_j/2\pi$ realizes the $|g\rangle \leftrightarrow |e\rangle$ rotation while the second pulse with the frequency of $(\omega_j - \alpha_j)/2\pi$ is a flip operation between $|e\rangle$ and $|f\rangle$ state, known as a e - f π rotation. After the initial state preparation, rectangular pulses are applied to open the qubit-resonator interaction for a time of about 205 ns. The control qubit Q_1 is biased to an optimized point close to ω_r , while the target qubit Q_2 stays on resonance with the resonator when a two-tone microwave pulse with the angular frequencies $\omega_r - \lambda_2 - \delta_1 - \delta_2$ and $\omega_{f,2} - \omega_r + \lambda_2 + \delta_1 + \delta_2$ are applied on Q_2 . Finally, the qubits are brought back to their idle points for quantum state tomography. To extract the density matrix, we use three tomographic operations $\{I, X/2, Y/2\}$

which are executed at the $\{|g\rangle, |e\rangle\}$ space after an e - f π rotation for each qubit, as can be seen in the third step of the sequence. For each tomographic operation, we perform the two-qubit joint readout by applying a two-tone measurement pulse to the transmission line, yielding the probabilities of the two-qubit basic states $\{|g\rangle, |e\rangle, |f\rangle\}^{\otimes 2}$. As only probabilities of $|g\rangle$ and $|f\rangle$ state are used for post analysis, the extracted density matrices have a trace value of smaller than 1, which indicates a leakage to the $|e\rangle$ state. In Fig. S5 we plot the measured leakage probability in $|e\rangle$ state for each qubit.

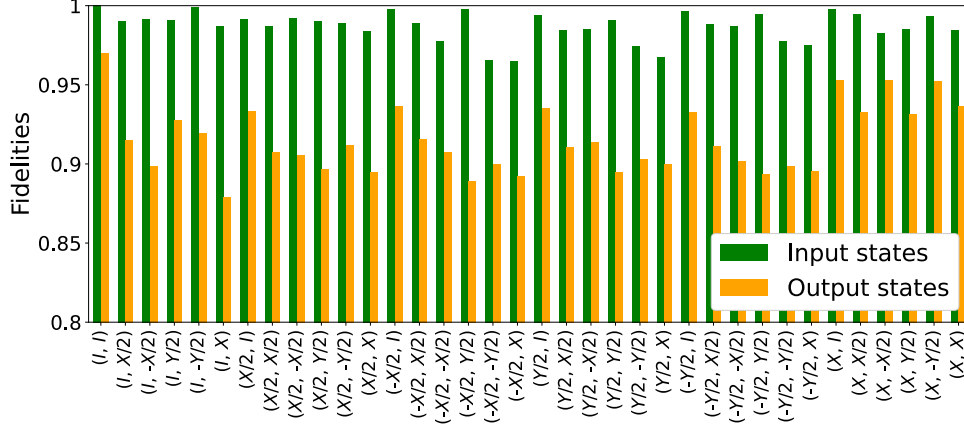


Fig. S6. The experimental fidelities of the input and output states, A total of 36 input and output states are used to perform the quantum process tomography. The labels in the x -axis represent the single qubit rotations used to prepare the initial states.

4. QUANTUM PROCESS TOMOGRAPHY

Quantum process tomography is executed by performing the state tomography for totally 36 input and corresponding output states after the gate sequence are applied. The input states are two-qubit product states

$$\{|g\rangle, \frac{1}{\sqrt{2}}(|g\rangle - i|f\rangle), \frac{1}{\sqrt{2}}(|g\rangle + i|f\rangle), \frac{1}{\sqrt{2}}(|g\rangle + |f\rangle), \frac{1}{\sqrt{2}}(|g\rangle - |f\rangle), |f\rangle\}^{\otimes 2} \quad (\text{S11})$$

which are produced by applying rotation pulses to each qubit. The mean fidelity characterized by quantum state tomography for all input states and output states are about 0.983 ± 0.003 and 0.915 ± 0.008 , respectively, as shown in Fig. S6. The χ -matrix can be extracted from these input and output states by utilizing the least square optimization method with the Hermitian and positive semidefinite constraints [9]. Note that we did not apply the constraint of unit trace for both the calculation of density matrix and χ -matrix considering the leakage to non-computational states.

5. GATE ERROR ANALYSIS

We have performed numerical simulation to quantify the errors of our gate. The infidelity of our gate mainly comes from the imperfect decoupling between the microwave drive and the qubit and also the decoupling between the qubit and the resonator. For example, when the control qubit Q_1 is in $|g\rangle$ state, the detuning between the microwave drive and the dressed state energy level is not large enough to decouple them, which induces a small transition from $|g_1, g_2, 0\rangle$ and $|g_1, f_2, 0\rangle$ to $|\Phi_1^0\rangle$ and $|\Phi_1^\pm\rangle$, leading to a leakage error. Lowering the drive amplitude can effectively reduce this leakage error, but will extend the evolution time and as a result increase the decoherence error. In addition, the nonlinearities a_j need to be larger to better decouple the control qubit Q_1 from the resonator and the target qubit when Q_1 is prepared in $|f\rangle$ state during the gate operation.

Considering all these factors, in Table S2, we numerically calculate the χ -fidelities for different nonlinearities and driving amplitudes. When decoherence is neglected, increasing the nonlinearity or decreasing the driving amplitude can both improve the fidelity, as shown in the last column of Table S2. The CNOT gate with χ -fidelity larger than 0.99 can be realized by use of qubits with

Table S2. Numerical results.

Nonlinearity, $\alpha_j/2\pi$ (GHz)	0.247	0.5	0.8	1.0	2.0	0.247	0.247	0.247	0.247	0.247	1.0
Driving amplitude, $\Omega_{ge,ef}/2\pi$ (MHz)	2.3	2.3	2.3	2.3	2.3	2.3	1.8	1.5	1.0	0.5	1.5
Gate time (ns)	209.5	220.4	220.1	223.5	223.8	209.5	281.0	360.5	532.5	1116.0	335.9
χ -fidelity with decoherence considered	0.908	0.932	0.942	0.944	0.945	0.908	0.906	0.892	0.884	0.799	0.935
χ -fidelity without decoherence considered	0.942	0.969	0.980	0.982	0.984	0.942	0.951	0.949	0.967	0.965	0.993

The gate fidelities for different nonlinearities and driving amplitudes are obtained by optimizing the evolution time and qubit frequencies. The cases with decoherence adopt the T_1 values listed in Table S1 and the pure dephasing times of about $40 \mu s$. The dephasing time used here is estimated from the exponential fit of the Ramsey measurement data before 200 ns. The first column presents numerical data considering parameters of our experimental device, which shows a good agreement with the experimental results. The limitation of nonlinearity, restriction of driving amplitude and decoherence contribute gate errors of about 4.2%, 2.3% and 3.4% respectively.

good coherence, provided the nonlinearity reaches $2\pi \times 1.0$ GHz and the driving amplitude reduces to $2\pi \times 1.5$ MHz. However, small driving amplitude requires long evolution time, which leads to more decoherence error. For a gate time of about 200 ns, the decoherence contributes about 3.4% of the total error, as shown in the table. To achieve a short evolution time, both the nonlinearity and coupling strength need to be enlarged. Our further numerical simulations show that, given parameters ($\alpha_j/2\pi = -3.69$ GHz, $\lambda_j/2\pi = 110$ MHz, $\Omega_{ge,ef}/2\pi = 5.9$ MHz, $T_{1,j}=60 \mu s$, $T_{2,j}^*=86 \mu s$) which are accessible in recent superconducting qubits [10–12], the CNOT gate with an optimized operation time of 87 ns yields an χ -fidelity of 0.991, indicating the potential of our scheme in high-fidelity quantum operations.

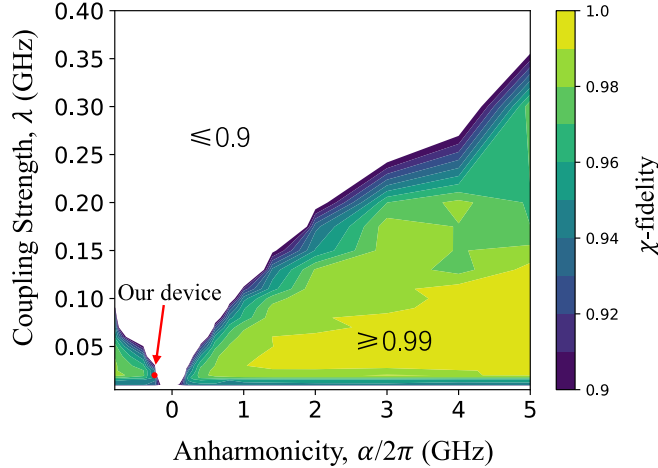


Fig. S7. Numerical process fidelities of the CNOT gate by varying the anharmonicity α_j and coupling strength λ_j . Here we have set $\alpha \equiv -\alpha_j$, $\lambda \equiv \lambda_j$ ($j = 1, 2$). The simulation results are obtained by optimizing the evolution time and qubit frequencies without considering decoherence. The red dot shows the position of our current device.

6. ADDITIONAL NUMERICAL SIMULATION

We have further performed numerical simulation by sweeping both the anharmonicity α_j and qubit-resonator coupling strength λ_j . For simplicity, the drive amplitude is fixed to be $\Omega_{ge,ef}/2\pi = 2.0$ MHz, similar to that used in our experiment. Fig. S7 plots the numerical process fidelities χ of the CNOT gate in parameter space, where the yellow region meets the threshold for surface code.

REFERENCES

1. C. Song, S.-B. Zheng, P. Zhang, K. Xu, L. Zhang, Q. Guo, W. Liu, D. Xu, H. Deng, K. Huang, D. Zheng, X. Zhu, and H. Wang, "Continuous-variable geometric phase and its manipulation for quantum computation in a superconducting circuit," *Nat. Commun.* **8**, 1061 (2017).
2. W. Ning, X.-J. Huang, P.-R. Han, H. Li, H. Deng, Z.-B. Yang, Z.-R. Zhong, Y. Xia, K. Xu, D. Zheng, and S.-B. Zheng, "Deterministic entanglement swapping in a superconducting circuit," *Phys. Rev. Lett.* **123**, 060502 (2019).
3. Z.-B. Yang, P.-R. Han, X.-J. Huang, W. Ning, H. Li, K. Xu, D. Zheng, H. Fan, and S.-B. Zheng, "Experimental demonstration of entanglement-enabled universal quantum cloning in a circuit," *npj Quantum Inf* **7**, 44 (2021).
4. C. Song, K. Xu, W. L., C.-P. Yang, S.-B. Zheng, H. Deng, Q. Xie, K. Huang, Q. Guo, L. Zhang, P. Zhang, D. Xu, D. zheng, X. Zhu, H. Wang, Y.-A. Chen, C.-Y. Lu, S. Han, and J.-W. Pang, "10-Qubit Entanglement and Parallel Logic Operations with a Superconducting Circuit," *Phys. Rev. Lett.* **119**, 180511 (2017).
5. E. Lucero, R. Barends, Y. Chen, J. Kelly, M. Mariani, A. Megrant, P. O'Malley, D. Sank, A. Vainsencher, J. Wenner, T. White, Y. Yin, A. N. Cleland, and John M. Martinis, "Computing prime factors with a Josephson phase qubit quantum processor," *Nat. Phys.* **8**, 719 (2012).
6. Q.-J. Guo, S.-B. Zheng, J. Wang, C. Song, P. Zhang, K. Li, W. Liu, H. Deng, K. Huang, D. Zheng, X. Zhu, H. Wang, C.-Y. Lu, and J.-W. Pang, "Dephasing-Insensitive Quantum Information Storage and Processing with Superconducting Qubits," *Phys. Rev. Lett.* **121**, 130501 (2018).
7. K. Xu, J.-J. Chen, Y. Zeng, Y.-R. Zhang, C. Song, W. Liu, Q. Guo, P. Zhang, D. Xu, H. Deng, K. Huang, H. Wang, X. Zhu, D. Zheng, and H. Fan, "Emulating Many-Body Localization with a Superconducting Quantum Processor," *Phys. Rev. Lett.* **120**, 050507 (2018).
8. D. Sank, "Fast, accurate state measurement in superconducting qubits," Ph. D. thesis, University of California Santa Barbara (2014).
9. M. Neeley, "Generation of three-qubit entanglement using Josephson phase qubits," Ph. D. thesis, University of California Santa Barbara (2010).
10. P. Jurcevic, A. J. Abhari, L. S. Bishop, I. Lauer, D. F. Bogorin, M. Brink, K. Capelluto, O. Günlük, T. Itoko, N. Kanazawa, A. Kandala, G. A. Keefe, K. Krsulich, W. Landers, E. P. Lewandowski, D. T. McClure, G. Nannicini, A. Narasgond, H. M. Nayfeh, E. Pritchett, M. B. Rothwell, S. Srinivasan, N. Sundaresan, C. Wang, K. X. Wei, C. J. Wood, J. B. Yau, E. J. Zhang, O. E. Dial, J. M. Chow, and J. M. Gambetta, "Demonstration of quantum volume 64 on a superconducting quantum computing system," *arXiv:2008.08571* (2020).
11. Y. Xu, J. Chu, J. Yuan, J. Qiu, Y. Zhou, L. Zhang, X. Tan, Y. Yu, S. Liu, J. Li, F. Yan, and D. Yu, "High-fidelity, high-scalability two-qubit gate scheme for superconducting qubits," *Phys. Rev. Lett.* **125**, 240503 (2020).
12. M. A. Yurtalan, J. Shi, G. J. K. Flatt, and A. Lupascu, "Characterization of multi-level dynamics and decoherence in a high-anharmonicity capacitively shunted flux circuit," *arXiv:2008.00593v1* (2020)